Molecular defects of the glycine 41 variants of alanine glyoxylate aminotransferase associated with primary hyperoxaluria type I

Barbara Cellini[a,1], Riccardo Montioli[a,1], Alessandro Paiardini[b], Antonio Lorenzetto[a], Fabio Maset[c], Tiziana Bellini[d], Elisa Oppici[a], and Carla Borri Voltattorni[a,2]

[a]Dipartimento di Scienze Morfologico-Biomediche, Sezione di Chimica Biologica, Facoltà di Medicina e Chirurgia, Università degli Studi di Verona, Strada Le Grazie, 8, 37134 Verona, Italy; [b]Dipartimento di Scienze Biochimiche "A. Rossi Fanelli" and Centro di Biologia Molecolare del Consiglio Nazionale delle Ricerche, Università "La Sapienza", 00185 Rome, Italy; [c]Dipartimento di Scienze Farmaceutiche, Università di Padua, via Marzolo 5, 35131 Padua, Italy; and [d]Dipartimento di Biochimica e Biologia Molecolare, Università di Ferrara, via Borsari 46, 44100 Ferrara, Italy

Edited by Gregory A. Petsko, Brandeis University, Waltham, MA, and approved December 31, 2009 (received for review July 31, 2009)

G41 is an interfacial residue located within the α-helix 34–42 of alanine:glyoxylate aminotransferase (AGT). Its mutations on the major (AGT-Ma) or the minor (AGT-Mi) allele give rise to the variants G41R-Ma, G41R-Mi, and G41V-Ma causing hyperoxaluria type 1. Impairment of dimerization in these variants has been suggested to be responsible for immunoreactivity deficiency, intraperoxisomal aggregation, and sensitivity to proteasomal degradation. However, no experimental evidence supports this view. Here we report that G41 mutations, besides increasing the dimer-monomer equilibrium dissociation constant, affect the protein conformation and stability, and perturb its active site. As compared to AGT-Ma or AGT-Mi, G41 variants display different near-UV CD and intrinsic emission fluorescence spectra, larger exposure of hydrophobic surfaces, sensitivity to Met53-Tyr54 peptide bond cleavage by proteinase *K*, decreased thermostability, reduced coenzyme binding affinity, and catalytic efficiency. Additionally, unlike AGT-Ma and AGT-Mi, G41 variants under physiological conditions form insoluble inactive high-order aggregates (~5,000 nm) through intermolecular electrostatic interactions. A comparative molecular dynamics study of the putative structures of AGT-Mi and G41R-Mi predicts that G41 → R mutation causes a partial unwinding of the 34–42 α-helix and a displacement of the first 44 N-terminal residues including the active site loop 24–32. These simulations help us to envisage the possible structural basis of AGT dysfunction associated with G41 mutations. The detailed insight into how G41 mutations act on the structure-function of AGT may contribute to achieve the ultimate goal of correcting the effects of these mutations.

dimer interface | pathogenic variant | protein aggregation | pyridoxal 5'-phosphate

Alanine:glyoxylate aminotransferase (AGT) is a homodimeric pyridoxal 5′-phosphate (PLP) dependent enzyme which catalyzes the interconversion of L-alanine and glyoxylate into pyruvate and glycine. Human AGT has been cloned, expressed in *E. coli* and purified. The enzyme crystal structure, complexed with the competitive inhibitor amino-oxyacetic acid, was determined at a resolution of 2.5 Å. Each subunit includes a N-terminal extension (residues 1–21), a large N-terminal domain (residues 22–282) containing the PLP-binding lysine (K209), and a smaller C-terminal domain (residues 283–392) (1). Steady-state and pre-steady-state kinetic studies featuring the AGT transamination revealed high specificity for glyoxylate to glycine processing, consistent with a key role of AGT in glyoxylate detoxification (2). The human liver-specific AGT is localized in the peroxisomal matrix (3). The enzyme has been the focus of extensive clinical research because its functional deficiency causes primary hyperoxaluria type 1 (PH1). PH1 is a rare autosomal recessive disorder characterized by excessive synthesis and excretion of oxalate and glycolate, and progressive accumulation of insoluble oxalate in the kidneys and urinary tract (4). The AGT gene (*AGXT*) occurs normally as one of the two allelic forms: the major (AGT-Ma) or minor (AGT-Mi) alleles. The latter, comprising two coding polymorphisms, P11L and I340M, and a noncoding duplication in intron 1 (5), has no dramatic effect on the properties of AGT. To date, well over 100 pathogenic mutations associated to AGT-Ma and/or AGT-Mi are known (6). Three categories of enzymatic phenotypes causing PH1 can be identified: deficiency of AGT catalytic activity but not AGT immunoreactivity, catalytic activity and immunoreactivity deficiency, and mistargeting to mitochondria (4, 7). Notably, clinical data for single PH1 AGT mutations are generally limited to a small number of individuals, which may interfere with identifying clear correlations between disease characteristics and properties of mutant proteins. Currently, the way of treatment of this progressive and potentially fatal disease is poor, as the molecular bases of the effects of the various disease-associated point mutations are unknown. In the last years, a biochemical characterization of the pathogenic variants G82E-Ma and F152I-Mi allowed us to correlate the clinical and enzymatic phenotypes with the structural and functional properties of the corresponding variants (2, 8).

The G41 series of pathogenic mutations, including the G41R encoded on the background of the major (G41R-Ma) and the minor (G41R-Mi) alleles, and the G41V, which only cosegregates with the major allele (G41V-Ma), is of special interest because (*i*) G41 is an interfacial residue making van der Waals contacts with the same residue of the other subunit and belongs to an α-helix connected with the active site loop 24–32 (Fig. S1), (*ii*) G41R mutation is more severe when it occurs on AGT-Mi than on AGT-Ma (4), and (*iii*) responsiveness to pyridoxine therapy for the patients bearing these mutations is so far unknown (9). Previous clinical and cell biochemical studies suggested that the weakening of the dimeric structure of AGT consequent to G41 replacements could be responsible for depletion of immunoreactive AGT, its intraperoxisomal aggregation (4, 10), and sensitivity to proteasomal degradation (11, 12). Because formal proves of the effect of these mutations at the molecular level are so far absent, we thought to provide insights into the molecular basis of the G41 mutation's pathogenicity. Biochemical data indicate that G41 mutations, besides causing a weakening of the intersubunit interaction, alter the conformational state of the AGT dimeric form, reduce its resistance to thermal inactivation

Author contributions: B.C., R.M., and C.B.V. designed research; B.C., R.M., A.P., A.L., F.M., T.B., and E.O. performed research; B.C., R.M., A.P., and C.B.V. analyzed data; C.B.V. wrote the paper.

The authors declare no conflict of interest.

This article is a PNAS Direct Submission.

[1]B.C. and R.M. contributed equally to this work.

[2]To whom correspondence should be addressed. E-mail: carla.borrivoltattorni@univr.it.

This article contains supporting information online at www.pnas.org/cgi/content/full/0908565107/DCSupplemental.

www.pnas.org/cgi/doi/10.1073/pnas.0908565107

and unfolding, and induce susceptibility to proteolytic degradation and self-aggregation. Moreover, predictions of the structural effects caused by G41 mutation by means of molecular dynamics (MD) provide a possible interpretation and explanation of our in vitro results.

Results

G41 Mutations Affect the Spectral Features and the Coenzyme Binding Affinity. Like AGT-Ma and AGT-Mi, G41 variants bind 2 mol of PLP per dimer, and exhibit visible absorbance and CD spectra similar to those of AGT-Ma or AGT-Mi, even if their absorbance and dichroic maxima are about 10–12 nm blue shifted (Fig. S2 and *Inset*). The $K_{D(PLP)}$ values for G41R-Ma, G41V-Ma, and G41R-Mi were found to be 1.5 ± 0.4, 0.55 ± 0.1, and 6.0 ± 0.5 μM, respectively, that are ∼6-, 2-, and 23-fold higher than that of AGT-Ma or AGT-Mi (2, 8). Both AGT-Ma and AGT-Mi bind pyridoxamine 5′-phosphate (PMP) with a $K_{D(PMP)}$ value $\ll 0.1$ μM, whereas even a prolonged time of incubation of the apo forms of G41 variants with PMP (up to 5 mM) does not result in a dichroic signal at 340 nm, typical of the AGT-PMP complex (2). Thus, G41 mutations exert a decrease in the PLP binding affinity and a dramatic reduction in the PMP binding affinity. The comparison of near-UV CD spectra as well as of intrinsic and 1-anilinonaphthalene sulfonic acid (ANS) fluorescence spectra of AGT-Ma, AGT-Mi, and G41 variants provides evidence that a different conformation exists between each apoenzymatic form and the corresponding holo form, and between the holo and apo forms of G41 variants and the corresponding forms of AGT-Ma or AGT-Mi (Fig. S3*A* and *B*). These data imply that (*i*) conformational changes seem to accompany the apo to holo transition for each enzymatic form, and (*ii*) G41 mutations affect the overall conformation of both holo and apo AGT.

The far-UV CD spectra of G41 variants have been compared with those of AGT-Ma and AGT-Mi. All spectra exhibit minima at 210 and 222 nm, typical of proteins containing appreciable amounts of α-helix. However, spectra deconvolution reveals that AGT-Ma, AGT-Mi, and G41V-Ma have an identical composition of the overall secondary structure, whereas both G41R-Ma and G41R-Mi display about 5% less α-helical content.

G41 Mutations Slightly Affect the Kinetic Parameters. The kinetic parameters of AGT-Ma, AGT-Mi, and G41 variants for the pair alanine-glyoxylate are reported in Table S1. The K_m values of G41 variants for L-alanine and glyoxylate are not significantly altered, whereas the k_{cat} values decrease by 1.5–3.5-fold as compared to those of the corresponding AGT-Ma and AGT-Mi. Altogether, these data indicate that the G41 mutations slightly affect the catalytic properties of AGT.

G41 mutations increase the dimer-monomer equilibrium dissociation constant (K_d). As a first step to investigate the impact of G41 mutations on the AGT dimeric structure, photo-induced cross-linking experiments with Tris(2,2′-bipyridyl) ruthenium(II) chloride (TBPR) have been carried out at 1 μM enzyme concentration. TBPR cross-linking is incomplete and also gives rise to the formation of aggregates and intramolecular cross-linked monomers. Nevertheless, it is possible to estimate the relative population of chemically cross-linked dimer to monomer with similar results for all the holo species, but lower for apo G41 variants than for apoAGT-Ma and apoAGT-Mi (Fig. S4). To validate these data we used the very accurate and sensitive size-exclusion chromatography (SEC) method. Holo and apo forms of AGT-Ma and AGT-Mi as well as the holo forms of the G41 variants from 5 to 0.1 μM concentration (the latter value being the detection limit), eluted as a single peak with a retention volume corresponding to a dimer. Thus, the K_d values of these species must be $\ll 0.1$ μM. On the other hand, the apo forms of G41 variants over the range $50 - 0.1$ μM enzyme concentration eluted as a single peak whose position varied between the dimeric and the monomeric forms of the enzyme, indicating a rapid equilibrium process. Plots of the percent dimer as a function of apoG41R-Ma and apoG41R-Mi concentrations give hyperbolic-like curves, the linear transformation of which yields the K_d values of 0.32 ± 0.05 and 1.8 ± 0.5 μM, respectively. In the case of apoG41V-Ma, a decrease of the integrated peak area starts at 1.5 μM reaching at 0.1 μM a value about 30% of the one expected, possibly because of monomerization followed by artefactual aggregation. A K_d value ranging from 1.5 to 0.1 μM can be estimated for this mutant. The SEC results, consistent with those of cross-linking analyses, do not allow to quantify the impact of G41 mutations on the K_d value of holoAGT, but clearly indicate that the mutations increase the K_d value of apoAGT.

G41 Mutations Induce Susceptibility to Proteinase *K* Digestion. Limited proteolysis was used to further probe that replacements of G41 change the overall conformation of AGT. AGT-Ma, AGT-Mi, and the G41 variants in the holo and apo forms were incubated in 100 mM potassium phosphate buffer, pH 7.4, at 25 °C with proteinase *K* at different AGT/protease weight ratios (from 5,000/1 to 100/1). When aliquots of these reaction mixtures were withdrawn at different times and subjected to SDS-PAGE, it was observed that, although the size of the band (∼42.7 kDa) corresponding to the intact holo or apo forms of AGT-Ma and AGT-Mi remains unaltered even after a prolonged time of incubation (Fig. S5*A*), that of G41 variants gradually decreases and simultaneously a faster migrating band (∼40.2 kDa) appears. Both the 42.7 and 40.2 kDa bands stain with antibody raised against the C-terminal hexahistidine tag, as revealed by Western blot analysis, indicating that the cleavage occurs within the N terminus. In fact, Maldi-mass spectrometry analysis yields a molecular weight difference for the N terminus truncated fragment of 5503 ± 15 atomic mass unit compared with the full-length G41R mutant, compatible with a cleavage site located at the peptide bond Met53-Tyr54. The effect of proteinase *K* on holo G41R-Mi is shown in Fig. 1, and that on holo G41V-Ma in Fig. S5*B*. The initial velocity values of the cleavage (expressed as μg enzyme/min/μg proteinase *K*) determined by measuring the decrease of the intensity of the band corresponding to the intact enzyme, are 4 ± 1, 530 ± 40, and 6 ± 1 for the holo forms of G41R-Ma, G41R-Mi, and G41V-Ma, respectively, and 130 ± 30, 870 ± 90, and 30 ± 6 for the corresponding apo forms. The proteolytic cleavage is accompanied by a time dependent loss of transaminase activity occurring for holoG41R-Mi with an initial velocity of 420 ± 50 μg mutant/min/μg proteinase *K*, a value that agrees with that of degradation. At a 10/1 AGT/proteinase *K* weight ratio, G41 variants are degraded in less than a half-hour to low molecular weight peptides, whereas AGT-Ma and AGT-Mi remain unaltered. Altogether these data indicate that, unlike

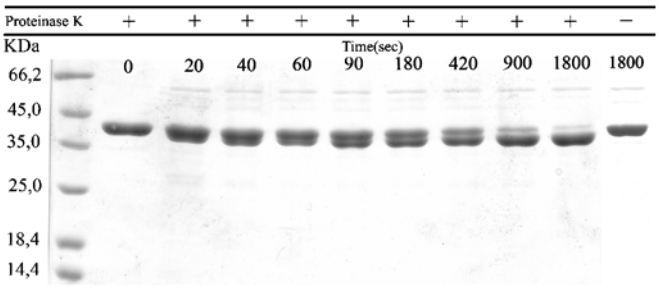

Fig. 1. Effect of proteinase *K* on holoG41R-Mi. HoloG41R-Mi (15 μM) was incubated at 25 °C in 100 mM potassium phosphate buffer, pH 7.4, at a 1,000/1 (wt/wt) mutant/proteinase *K* ratio. At times indicated, aliquots were removed, treated (see *Methods*), and subjected to 12% SDS-PAGE. Plus and minus signs indicate presence or absence of proteinase *K*.

AGT-Ma and AGT-Mi, G41 variants undergo digestion and concomitant inactivation more pronounced for their apo than for the corresponding holo forms.

G41 mutations induce formation of high order inactive aggregates. We noticed that, unlike AGT-Ma and AGT-Mi, holoG41 variants at an ionic strength (I) value lower than 260 mM and/or at an enzyme concentration higher than 10 μM form visible insoluble aggregates. When these solutions are centrifuged, a yellow pellet indicative of PLP-bound aggregates appears. The specific activity of the precipitates resuspended in the assay buffer is <5% than that of the supernatant containing the dimeric species. This observation, together with the documented presence of intraperoxisomal aggregates in patients bearing G41R mutation (10), led us to investigate in some detail this phenomenon by means of turbidimetry and dynamic light scattering (DLS) studies under physiological conditions, i.e., at 37 °C, pH 7.4 at I = 150 mM. As shown in Fig. 2, significant changes in turbidity began after a lag phase ranging from 50 to 120 min for both the holo and apo forms of G41R-Mi as well as for the apo forms of G41R-Ma and G41V-Ma. No turbidity could be detected for these enzymatic species at pH 7.4, and I = 260 mM at either 25 °C or 37 °C at least over a 5 h interval. Fig. 3*A* and *B* show plots of the total count rate as a function of time for holo and apoenzymes of AGT-Ma, AGT-Mi, and G41 variants. The increase in count rate for the holo and apo forms of AGT-Ma and AGT-Mi is very slow, whereas the more typical fast aggregation for G41 variants could be seen with the count rate leveling off after ~20–40 min. The decrease in the light scattering intensity occurring for holoG41R-Mi and for the apo forms of G41 variants is due to precipitation of the protein aggregates. Altogether, the turbidity and DLS data indicate that (*i*) replacements of G41 are responsible for the propensity of mutants to self-association, the extent of which is more pronounced for the apo forms than for the corresponding holo forms, and (*ii*) G41R-Mi results the variant most prone to aggregation. The molecular size of the species present in the enzymic solutions has been also evaluated. The particle size of the dimeric form of AGT-Ma, AGT-Mi, and G41 variants, measured at 25 °C, pH 7.4, at I = 260 mM, i.e., under conditions of no detectable association, is about 10 nm. This value is consistent either with that (9.32 nm) derived from the X-ray structure (1) or that (7 ± 2 nm) calculated by an appropriate empirical equation (13). When the aggregation process occurring under the physiological conditions mentioned above was followed by DLS,

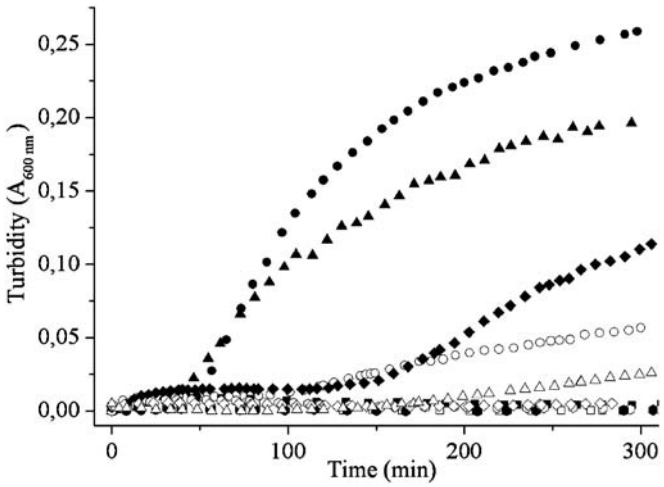

Fig. 2. Time dependence of turbidity of AGT-Ma, AGT-Mi, and G41 variants. Absorbance at 600 nm as a function of time of 4 μM apo forms of AGT-Ma (■), AGT-Mi (▼), G41R-Ma (▲), G41V-Ma (◆), and G41R-Mi (•) in potassium phosphate buffer, pH 7.4, I = 150 mM at 37 °C. Corresponding holoenzymes, open symbols.

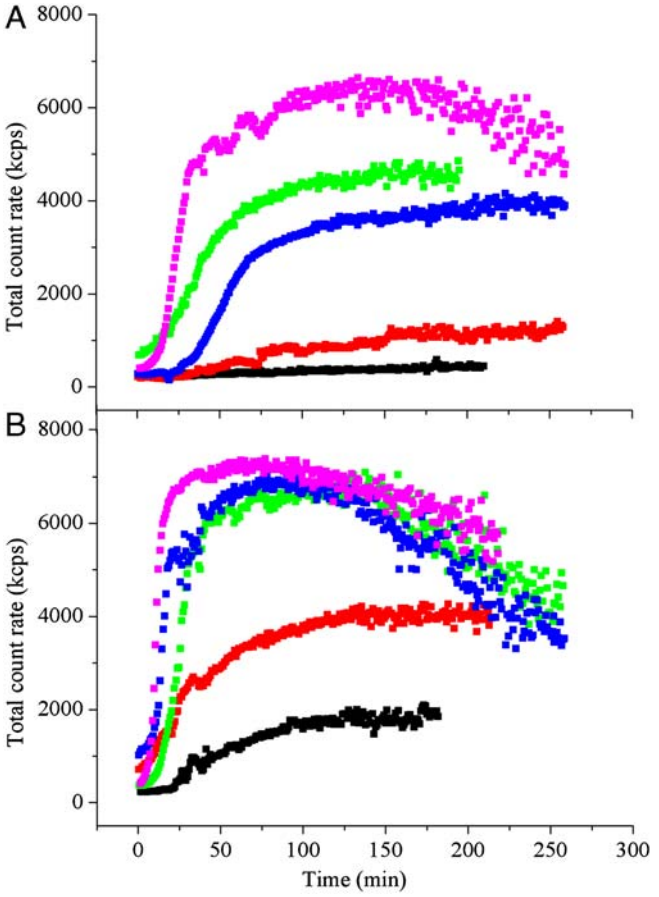

Fig. 3. Time-dependence of total count rate (measured as kilo counts per second) of AGT-Ma, AGT-Mi, and G41 variants in the holo (*A*) and apo (*B*) forms. Measurements performed at 4 μM enzyme concentration, 37 °C, I = 150 mM, pH 7.4. Color code: black, AGT-Ma; red, AGT-Mi; blue, G41R-Ma; green, G41V-Ma; fuchsia, G41R-Mi.

the time dependence of the apparent particle size indicates that the 10 nm species is always present for holo and apo AGT-Ma and holoAGT-Mi, although small aggregates (100–800 nm) appear after about 30 min (Fig. 4*A* and *B*). Considering that the scattering intensity is proportional to the sixth power of the particle diameter, the dimer must be in these species very abundant in number. In contrast, the dimer disappears over a 5–75 min time range, depending on the enzymatic species, for AGT-Mi in the apo form and for G41 variants in both the holo and apo forms. Moreover, whereas only small aggregates (100–800 nm) accumulate in apoAGT-Mi, in G41 variants a distinct population of higher-order aggregates (~5,000 nm), along with small aggregates, can be identified (Fig. 4*B–E*). From these data it can be also envisaged that (*i*) the turbidity is mainly associated to the presence of high-order aggregates, and (*ii*) the lack of detectable turbidity for G41R-Ma and G41V-Ma in the holo form could be ascribed to the very low fractional contribution of the larger particles to the total scattering intensity.

The effect of 200 mM trimethylamine-N-oxide (TMAO) or 100 mM betaine [two osmolytes known to suppress protein aggregation (14)] on the aggregation process of holoG41R-Mi has been followed by DLS. Either TMAO or betaine, although unable to decrease the amount of and size of the aggregates formed at equilibrium, as detected by the final count rate leveling off, cause a slight increase in the lag time duration (from 10 to 20 min) and in the persistence of the dimeric species (from 35 to 70 min) in the aggregation kinetics.

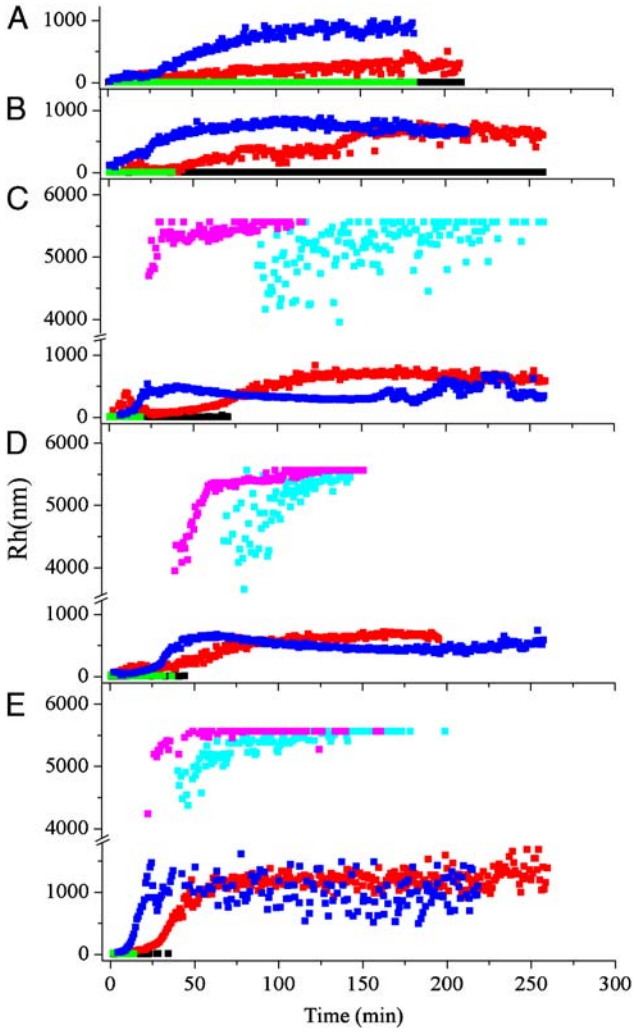

Fig. 4. Time dependence of the apparent diameters of AGT-Ma, AGT-Mi, and G41 variants. Experimental conditions (see legend to Fig. 3). (*A*) holo and apo AGT-Ma. (*B*) holo and apo AGT-Mi. (*C*) holo and apo G41R-Ma. (*D*) holo and apo G41V-Ma. (*E*) holo and apo G41R-Mi. Color code: black, holo dimer; green, apo dimer; red, holo small aggregates; blue, apo small aggregates; cyan, holo high aggregates; fuchsia, apo high aggregates.

G41 Mutations Decrease Resistance to Thermal Denaturation and Inactivation. A differential calorimetric study (DSC) was carried out to reveal the impact of G41 mutations against thermal denaturation. Thermal denaturation of holo and apo forms of AGT-Ma, AGT-Mi, G41R-Ma, and G41V-Ma as well as of holo form of G41R-Mi produces DSC profiles consisting of an endothermic transition due to the protein denaturation followed by a large exothermic transition due to the aggregation of the denaturated protein (Fig. S6), precluding the peaks deconvolution. Thus, the maxima of the endothermic transitions of these species represent apparent melting temperature (Tm) values. The Tm of apoG41R-Mi could not be determined because of the lack of an observable transition, possibly due to overlapping of the denaturation and aggregation processes (Table 1). The thermal effect on the catalytic function of AGT-Ma, AGT-Mi, and G41 variants was also measured, and the transition midpoints of thermal inactivation (Ti) are reported in Table 1. The results indicate that (*i*) holo AGT-Ma, AGT-Mi, and G41 variants display Tm and Ti values higher than those of the corresponding apoenzymes, which supports different conformational states of holo and apo forms, (*ii*) AGT-Ma is more resistant than AGT-Mi, and (*iii*) G41 mutations decrease the thermal stability, being G41R-Mi the most thermally instable variant.

Table 1. Transition midpoints of thermal denaturation (Tm) and inactivation (Ti) of AGT-Ma, AGT-Mi, and G41 variants

Enzyme	Holo form	Apo form	Holo form	Apo form
	Tm*, °C		Ti†, °C	
AGT-Ma	77.3	62.4	77.4	59.1
AGT-Mi	73.2	55.6	72.6	52.2
G41R-Ma	60.3	57.6	57.7	53.0
G41R-Mi	53.7	ND	51.8	46.0
G41V-Ma	61.0	58.3	62.3	54.5

ND, not detectable.

*They represent apparent Tm values and are the mean of two independent experiments. The error is within ±0.3 °C error.

†Data inactivation points were subjected to nonlinear regression analysis and Ti values were calculated. The data are the means of at least two independent experiments. The standard error of the mean was less than 5% of the mean value in every case.

MD studies. We examined in a comparative way the conformational space sampled by the putative structures of AGT-Mi and G41R-Mi by high-temperature (500 K) MD simulations with explicit water solvation. Both AGT-Mi and G41-Mi reach an equilibrated state after ~100 ps (Fig. S7*A*), thereafter their global architecture remaining stable, as confirmed by the indicators commonly used to analyze MD simulations (Fig. S7*A–C*). Unlike that observed for AGT-Mi, a marked fluctuation can be observed for the region spanning residues 1–44 of both monomers of G41R-Mi. This region comprises the active site loop (residues 24–32) and the α-helix 34–42 in which the G41R substitution takes place. In particular, the MD simulation of G41R-Mi reveals that the N-terminal α-helices (residues 34–42) undergo a progressive displacement (Fig. S8), and a partial unwinding of the first and second turns

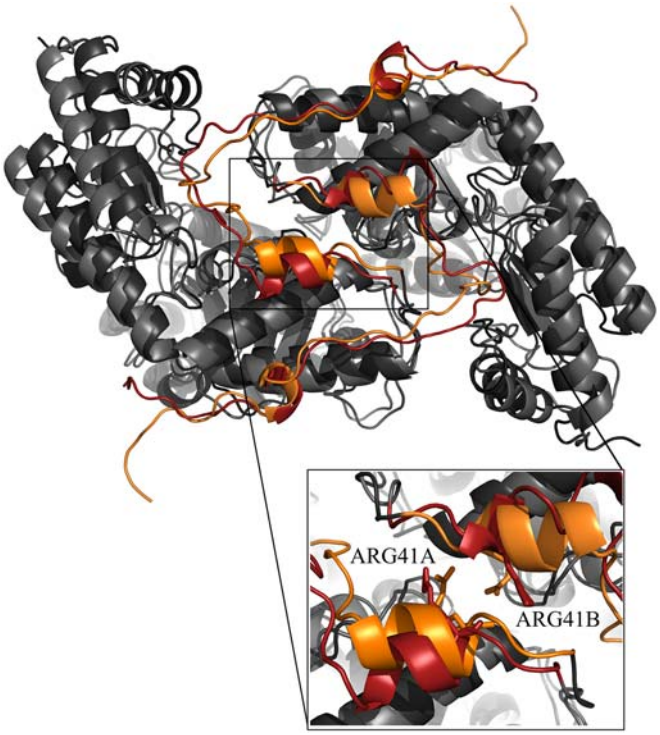

Fig. 5. Comparison of the initial 3D model of G41R-Mi (dark gray) with the averaged structure obtained from MD simulation (light gray). Residues 1–46, roughly corresponding to the N-terminal arm of G41R-Mi, are highlighted in orange for the initial 3D model and in red for the averaged structure. (*Inset*) Detail of the α-helix in which the G41R substitution takes place (residues 34–42).

of the helix (Fig. 5). It is likely that these events could be related to the accommodation of the long side chain of Arg41.

Discussion

G41, located at the end of the α-helix 34–42 of AGT, is an interfacial residue which makes van der Waals contacts with the same residue of the adjacent subunit (1). Thus, it is not surprising that (*i*) the conversion of the small, uncharged Gly41 to the bulky, charged Arg causes a ∼5% loss of α-helix content, while the conversion to Val, a larger uncharged residue, does not have a detectable effect on the overall secondary structure, and (*ii*) the apo forms of G41 variants undergo reversible dissociation of the subunits with K_d values from at least ∼3-fold to ∼20-fold higher than that of apoAGT-Ma or apoAGT-Mi. Actually, we found that G41 variants in the dimeric form differ from AGT-Ma or AGT-Mi under many respects. Their structural conformation and stability are altered, as detected by difference in the near-UV CD and intrinsic emission fluorescence spectra, larger exposure of hydrophobic surfaces, sensitivity to proteinase *K* cleavage, and decrease in Tm and Ti with respect to AGT-Ma and AGT-Mi. Additionally, G41 variants show slightly altered visible spectroscopic features, a reduced steady-state catalytic activity, and a decreased PLP binding affinity as well as a dramatic reduction in the PMP binding ability.

A comparative study of the putative structures of AGT-Mi and G41R-Mi by MD predicts that the G41R mutation would cause the partial unwinding of the α-helix 34–42 as well as the displacement of the N-terminal arm and its exposure to the environment. Although these predictions are of course not an experimental evidence of the structural effects caused by the mutation, they are consistent with the in vitro data of G41R-Mi, i.e., the 5% loss of the α-helix content and the susceptibility of the Met53-Tyr54 peptide bond to proteinase *K* cleavage. It is worth noting that, although G41 is far from the active site, it is located in the α-helix connected with the active site loop (residues 24–32) belonging to the N terminus (Fig. S1). Therefore, we might speculate that the alterations of the visible spectroscopic and catalytic features of G41 variants could be due to the rearrangements occurring around the mutated residue transmitted to the active site.

Another particularly interesting aspect is that, unlike AGT-Ma and AGT-Mi, G41 variants spontaneously form insoluble inactive high-order aggregates (∼5,000 nm) under physiological conditions of temperature, I and pH. The finding that the aggregation extent greatly decreases as I increases may be ascribed to the reduction in favorable attractive interactions due to screening effects. This behavior indicates that aggregation is not due to hydrophobic interactions, in which case the addition of salt would enhance aggregation and little effect would be seen at low I, but rather to electrostatic intermolecular interactions arising from protein charge heterogeneity. It is also worth noting that the aggregation occurs at a pH value lower than pI, thus excluding an isoelectric precipitation. Why are the G41 variants aggregation prone? In the absence of the crystal structure of these variants, the protein electrostatic potential distribution for AGT-Mi and the 1–44 N-terminus lacking form of AGT-Mi has been calculated by electrostatic computer modeling. The truncated form was chosen for comparison because it would mimic the structure of G41R-Mi upon the displacement of the N-terminal arm. As shown in Fig. 6*A* and *B*, AGT-Mi displays a highly positive charge distribution around its surface, whereas the truncated form exhibits a clear dipole segregation of charges. In fact, the depletion of the highly positively charged N-terminal arm of AGT-Mi leads to the exposure of several negatively charged residues (Asp51, Glu59, Glu62, Glu274, Glu281, Asp344, Glu346 of each monomer), i.e., to a condition of electrostatically driven self-aggregation of AGT. Thus, one can reason out that the fluctuation of the N terminus in G41R-Mi could cause the exposure of negative charged residues similar to that observed for the truncated AGT form. Although this could be a plausible explanation for the propensity of G41 variants to aggregate spontaneously, a conclusive evidence for this interpretation is lacking.

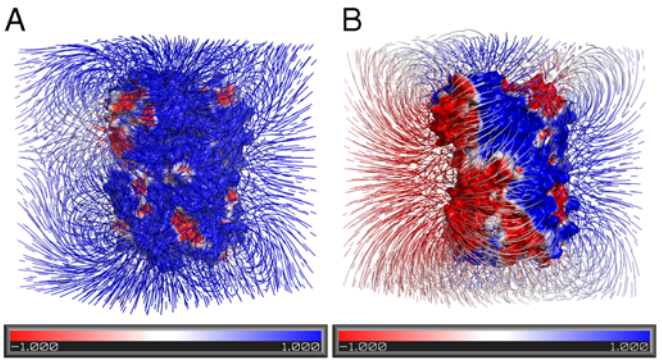

Fig. 6. Electrostatic potential surface maps of AGT-Mi and its truncated form. Electrostatic gradient and map (kT/e) of AGT-Mi (*A*), and 1–44 truncated form of AGT-Mi (*B*).

The finding that G41R-Mi displays structural and functional alterations more pronounced than G41R-Ma needs to be discussed. The thermal unfolding data indicate that the instability of G41R-Mi is due to the additive contribution of the polymorphic and pathogenic mutations. The effect of the polymorphic substitutions is possibly due to P11L in that Pro instead of Leu (*i*) contributes to the increase of structural rigidity, (*ii*) exerts additional constraints to the backbone, because the ring closure keeps its Φ angle value almost fixed, and (*iii*) makes hydrophobic interactions with a surface cavity surrounded by residues Leu14, Glu62, Gly63, Tyr66, and Ala280.

Altogether, our data assist in assessing a picture of the G41 variants enzymatic phenotype more exhaustive than that previously proposed. The pathogenicity of G41 variants has been until now related to a disruption of the interface and impairment of dimerization resulting in formation of monomers with reduced catalytic activity and prone to degradation and/or intraperoxisomal aggregation (1, 4, 15). Our in vitro results would indicate not only the impact of G41 mutations on the dimerization but also provide evidence that G41 variants in the dimeric form are prone to degradation and aggregation. The presence of aggregates only within the peroxisomal matrix in patients bearing G41R mutation (10) is consistent with this view in that the peroxisomal import machinery acts on folded dimeric proteins. In any case, it will be important to establish if the intraperoxisomal aggregates have ultrastructure similarities with the aggregates spontaneously formed in vitro. If this were the case, the electrostatically driven protein aggregation between folded dimers could represent a unique pathogenic mechanism by which G41 inherited mutations would cause protein aggregation. Indeed, many disease-related genetic mutations are known to alter the folding or stability of proteins leading to intermediates in which hydrophobic patches become exposed and prone to self-association.

Overall, our work improves the understanding of the correlation between the genotype and the enzymatic phenotype, thus allowing us to foresee the response to pyridoxine in patients carrying the G41 mutations. Administration of pyridoxine to these patients is not sufficient to counteract the disease because the molecular defects of these variants appear to be related to structural rearrangements yielding molecules that are both in the apo and the holo forms prone to degradation and aggregation. A promising therapeutic strategy could be the administration of small molecules able to stabilize the native state of the protein, thus preventing degradation and aggregation. In this regard, our preliminary results on the effects of osmolytes on the aggregation behavior of G41 variants could be an encouraging perspective.

Methods

Construction, Expression and Purification of G41 Variants. AGT-Ma and AGT-Mi were prepared as reported (2, 8). Site-directed mutagenesis, expression, and purification of G41 variants in the C-terminal His-tagged form were performed using standard procedures as described in *SI Text*.

Enzyme Activity Assays. Pyruvate formation was measured by the spectrophotometric assay already reported (2). Kinetic parameters for the pair alanine/glyoxylate of G41 variants were determined in the presence of 150 μM PLP by varying the substrate concentrations at a fixed saturating cosubstrate concentration. Data were fitted to the Michaelis–Menten equation. Thermal inactivation experiments were performed as follows: enzyme (10 μM) was incubated for 10 min in 100 mM potassium phosphate buffer, pH 7.4, at different temperatures, and then chilled on ice. Transaminase activity was measured as indicated above.

Binding Affinity for PLP. The $K_{D(PLP)}$ of G41 variants were determined by measuring the PLP-induced changes either on the intrinsic fluorescence or in the CD visible spectrum of the apoenzymes. The experimental conditions and the relative data analysis are given in *SI Text*.

Cross-Linking and SEC Experiments. Photo-induced cross-linking with TBPR was performed as previously described (7). SEC experiments were done on an Akta FPLC system (GE Healthcare) using a custom packed Sephacryl S-300 10/600 column. The data were analyzed according to the method of Manning et al. (16). Details are given in *SI Text*.

Proteinase *K* Digestion and Mass Spectrometry Analysis. Holo and apo AGT-Ma, AGT-Mi, and G41 variants (15 μM) were treated with proteinase *K* in 100 mM potassium phosphate buffer, pH 7.4, at 25 °C at various AGT/proteinase *K* (wt/wt) ratios. At various times, 15 μL-aliquots were withdrawn from the reaction mixtures and subjected to enzymatic activity assay, SDS-PAGE, and immunoblotting. The reaction was stopped by adding PMSF or EGTA to a final concentration of 2 mM to each aliquot. After staining with Coomassie blue, the band intensities were visualized and analyzed using ImageJ software (Wajne Rasband). Immunoblotting was made as described in *SI Text*. Liquid-chromatography/MS analyses of G41R-Mi were carried out with a model Mariner Esi-Tof spectrometer from PerSeptive Biosystems, connected to a C4 Grace-Vydac microbore column (1 × 50 mm). Column elution was carried out with a CH_3CN-1% HCOOH gradient from 1 to 80% in 30 min. Proteolysis reaction of G41R-Mi with proteinase *K* was analyzed with a model 4800 Plus Maldi-Tof-Tof instrument from Applied Biosystems. Samples were desalted on a P10 C4 Zip-Tip, eluted with a sinapinic acid (Sigma) saturated solution (2 μL) in $CH_3CN:H_2O$ (60:40 by vol). Details are given in *SI Text*.

Turbidimetry Measurements. The aggregation experiments were carried out in potassium phosphate buffer, pH 7.4, at different I values and/or different enzyme concentrations. The turbidity was monitored by measuring the absorbance at 600 nm as already reported (17).

DLS Measurements. DLS measurements were made on a Zetasizer Nano S device from Malvern Instruments. The temperature of sample cell was controlled by a thermostating system within ±0.1 °C and 12.5 × 45-mm disposable cells with stopper were used. To study the aggregation kinetics, an aliquot of each enzymatic species was diluted to a final concentration of 4 μM in potassium phosphate buffer pH 7.4 at the desired I and temperature. PLP was added to the holoenzyme solutions to a final concentration of 60 μM. The buffer was filtered immediately before use to eliminate any impurities. TMAO or betaine were added to the buffer before the addition of G41R-Mi.

Spectroscopic Measurements. Absorption, fluorescence, and CD spectra were performed as described in *SI Text*.

DSC. DSC experiments were conducted with a VP-DSC microcalorimeter (Microcal) in the temperature interval from 20 to 90 °C, with a scan rate of 90 °C/h in 100 mM potassium phosphate buffer, pH 7.4, and at 5.5 μM protein concentration.

Computational Analyses. MD simulations of the molecular models of AGT-Mi and G41R-Mi, derived from the crystal structure of human AGT (1), downloaded from Brookhaven Protein Data Bank (18) were performed. A detailed description of the generation of these structures and MD simulations is given in *SI Text*. Electrostatic computations on AGT-Mi and its N terminus deleted form were carried out by solving the nonlinear Poisson–Boltzmann equation, one of the most popular continuum models for describing electrostatic interactions between molecular solutes in salty, aqueous media. Adaptive Poisson Boltzman Solver was used to this purpose (19), with a protein and solvent dielectric of 2.0 and 80.0, respectively, and I = 150 mM.

ACKNOWLEDGMENTS. We gratefully acknowledge experimental contribution and advice by V. De Filippis, O. Marin, G. Arrigoni, and F. Dallocchio. Work was supported by grants from the Oxalosis and Hyperoxaluria Foundation and M.I.U.R. (PRIN 2007) (to C.B.V.).

1. Zhang X, et al. (2003) Crystal structure of alanine:glyoxylate aminotransferase and the relationship between genotype and enzymatic phenotype in primary hyperoxaluria type 1. *J Mol Biol* 331(3):643–652.
2. Cellini B, Bertoldi M, Montioli R, Paiardini A, Borri Voltattorni C (2007) Human wild-type alanine:glyoxylate aminotransferase and its naturally occurring G82E variant: Functional properties and physiological implications. *Biochem J* 408(1): 39–50.
3. Motley A, et al. (1995) Mammalian alanine/glyoxylate aminotransferase 1 is imported into peroxisomes via the PTS1 translocation pathway. Increased degeneracy and context specificity of the mammalian PTS1 motif and implications for the peroxisome-to-mitochondrion mistargeting of AGT in primary hyperoxaluria type 1. *J Cell Biol* 131(1):95–109.
4. Danpure CJ (2005) Molecular etiology of primary hyperoxaluria type 1: New directions for treatment. *Am J Nephrol* 25(3):303–310.
5. Purdue PE, Takada Y, Danpure CJ (1990) Identification of mutations associated with peroxisome-to-mitochondrion mistargeting of alanine/glyoxylate aminotransferase in primary hyperoxaluria type 1. *J Cell Biol* 111(6 Pt 1):2341–2351.
6. Coulter-Mackie MB, Rumsby G (2004) Genetic heterogeneity in primary hyperoxaluria type 1: Impact on diagnosis. *Mol Genet Metab* 83(1–2):38–46.
7. Lumb MJ, Danpure CJ (2000) Functional synergism between the most common polymorphism in human alanine:glyoxylate aminotransferase and four of the most common disease-causing mutations. *J Biol Chem* 275(46):36415–36422.
8. Cellini B, Montioli R, Paiardini A, Lorenzetto A, Voltattorni CB (2009) Molecular insight into the synergism between the minor allele of human liver peroxisomal alanine:glyoxylate aminotransferase and the F152I mutation. *J Biol Chem* 284(13): 8349–8358.
9. Coulter-Mackie MB, Lian Q, Wong SG (2005) Overexpression of human alanine: glyoxylate aminotransferase in *Escherichia coli*: Renaturation from guanidine-HCl and affinity for pyridoxal phosphate co-factor. *Protein Expres Purif* 41(1):18–26.
10. Danpure CJ, et al. (1993) Enzymological and mutational analysis of a complex primary hyperoxaluria type 1 phenotype involving alanine:glyoxylate aminotransferase peroxisome-to-mitochondrion mistargeting and intraperoxisomal aggregation. *Am J Hum Genet* 53(2):417–432.
11. Coulter-Mackie MB, Lian Q (2008) Partial trypsin digestion as an indicator of mis-folding of mutant alanine:glyoxylate aminotransferase and chaperone effects of specific ligands. Study of a spectrum of missense mutants. *Mol Genet Metab* 94(3):368–374.
12. Coulter-Mackie MB, Lian Q (2006) Consequences of missense mutations for dimerization and turnover of alanine:glyoxylate aminotransferase: Study of a spectrum of mutations. *Mol Genet Metab* 89(4):349–359.
13. Wilkins DK, et al. (1999) Hydrodynamic radii of native and denatured proteins measured by pulse field gradient NMR techniques. *Biochemistry* 38(50):16424–16431.
14. Venkatesu P, Lee MJ, Lin HM (2007) Thermodynamic characterization of the osmolyte effect on protein stability and the effect of GdnHCl on the protein denatured state. *J Phys Chem B* 111(30):9045–9056.
15. Danpure CJ (2006) Primary hyperoxaluria type 1: AGT mistargeting highlights the fundamental differences between the peroxisomal and mitochondrial protein import pathways. *Biochim Biophys Acta* 1763(12):1776–1784.
16. Manning LR, Dumoulin A, Jenkins WT, Winslow RM, Manning JM (1999) Determining subunit dissociation constants in natural and recombinant proteins. *Methods Enzymol* 306:113–129.
17. Yong YH, Foegeding EA (2008) Effects of caseins on thermal stability of bovine beta-lactoglobulin. *J Agric Food Chem* 56(21):10352–10358.
18. Sussman JL, et al. (1998) Protein data bank (PDB): Database of three-dimensional structural information of biological macromolecules. *Acta Crystallogr D* 54(Pt 1, Pt 6): 1078–1084.
19. Baker NA, Sept D, Joseph S, Holst MJ, McCammon JA (2001) Electrostatics of nanosystems: Application to microtubules and the ribosome. *Proc Natl Acad Sci USA* 98(18):10037–10041.